Nanoscale

RSC Publishing

PAPER

View Article Online
View Journal | View Issue

Cite this: *Nanoscale*, 2013, **5**, 4270

Dandelion-shaped nanostructures for enhancing omnidirectional photovoltaic performance

Shou-Yi Kuo,*[a] Ming-Yang Hsieh,[a] Hau-Vei Han,[b] Fang-I Lai,*[cd] Yu-Lin Tsai,[b] Jui-Fu Yang,[ac] Tsung-Yeh Chuang[e] and Hao-Chung Kuo*[b]

Received 30th January 2013
Accepted 7th March 2013

DOI: 10.1039/c3nr00526g

www.rsc.org/nanoscale

Broadband and omnidirectional light harvesting is important in photovoltaic technology because of its wide spectral range of radiation and the sun's movement. This study reports the fabrication and characterization of zinc oxide (ZnO) dandelions on $Cu(In,Ga)Se_2$ (CIGS) solar cells. The fabrication of dandelions involves the combination of self-assembled polystyrene (PS) nanospheres and the hydrothermal method, which is one of the simplest and cheapest methods of fabricating a three-dimensional, closely packed periodic structure. This study also investigates the optimization on dimension of the PS nanospheres using the rigorous coupled-wave analysis (RCWA) method. This study uses an angle-resolved reflectance spectroscope and a homemade rotatable photo *I–V* measurement to investigate the omnidirectional and broadband antireflections of the proposed dandelion structure. Under a simulated one-sun condition and a light incident angle of up to 60°, cells with ZnO dandelions arrays enhanced the short-circuit current density by 31.87%. Consequently, ZnO dandelions are suitable for creating an omnidirectionally antireflective coating for photovoltaic devices.

Introduction

Solar cells represent one of the most renewable and secure types of existing energy sources.[1] Based on their structure, solar cells can be roughly divided into bulk and thin film devices. Among all thin film solar cells, $Cu(In,Ga)Se_2$ (CIGS) and its related materials have become promising candidates for thin-film solar cells because of their high optical absorption, adjustable band-gap, and stable photo-degradation.[2,3] The conversion efficiencies of CIGS solar cells at the laboratory scale have exceeded 20%.[4]

Antireflective coatings (ARCs) play a particularly important role in solar cells, and can be applied to the surface of a material to reduce Fresnel reflection loss at the material interface.[5,6] Typical conventional multi-layered ARCs consist of a quarter wavelength stack of thin film dielectric layers with various refractive indices. However, multi-layered ARCs have some disadvantages, such as material selection, layer thickness control, thermal expansion mismatch, and material diffusion.[7,8] Over the past decade, sub-wavelength structures (SWSs) have been widely researched as replacements for multi-layered ARCs.[9,10] Biomimetic moth-eye structures and random nanorods have demonstrated excellent broadband and omni-directional antireflection characteristics. Fabrication processes involving electron beam lithography and dry etching have been widely used to fabricate various moth-eye structures in the past few years.[11] However, these fabrication processes are unsuitable for the mass production of nanostructures on large-area solar cells because the process-induced surface recombination defects decrease the device performance.[12–14] Consequently, nanostructures fabricated using bottom-up growth methods have been developed for device applications. These methods include molecular beam epitaxy,[15] vapor–liquid–solid growth,[16] and chemical vapor deposition.[17] However, these methods have some disadvantages, such as expensive equipment and high vacuum and temperature conditions.

ZnO is a wide-direct band gap material for 3.37 eV semiconductors, and has been used in several ZnO structures as ARCs, including nanowires,[18] nanorods,[19,20] nanotubes,[21] and nanobelts.[22] This study investigates a scalable and inexpensive bottom-up approach for self-assembling PS nanospheres on CIGS solar cells, and growing ZnO nanorods on PS nanospheres using a hydrothermal method. This is one of the simplest and fastest methods of fabricating a 2-D period structure using the

[a]*Department of Electronic Engineering, Chang Gung University, 259 Wen-Hwa 1st Road, Kwei-Shan, Taoyuan 333, Taiwan. E-mail: sykuo@mail.cgu.edu.tw; Fax: +886-3-2118507; Tel: +886-3-2118800 ext. 3744*

[b]*Institute of Electro-Optical Engineering, National Chiao-Tung University, 1001 University Road, Hsinchu, 300, Taiwan. E-mail: hckuo@faculty.nctu.edu.tw; Fax: +886-3-5735601; Tel: +886-3-571-2121 ext. 56304*

[c]*Department of Photonics Engineering, Yuan-Ze University, 135 Yuan-Tung Road, Chung-Li, 32003, Taiwan. E-mail: filai@saturn.yzu.edu.tw; Fax: +886-3-4514281; Tel: +886-3-4638800 ext. 7516*

[d]*Advanced Optoelectronic Technology Center, National Cheng Kung University, Tainan 701, Taiwan*

[e]*Department of Electro-Physics, National Chiao-Tung University, 1001 University Road, Hsinchu, 300, Taiwan*

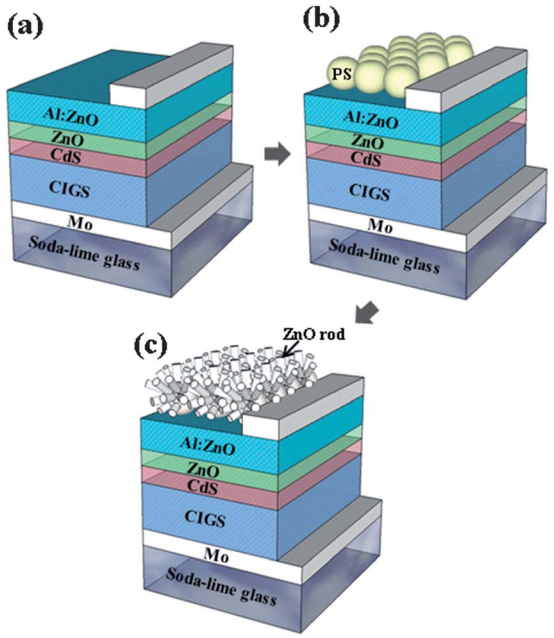

Fig. 1 Schematic process for fabricating the dandelion structures on the CIGS solar cell, (a) with PS nanospheres, (b) with ZnO dandelions.

self-assembled PS nanospheres.[23] Growing ZnO nanorods using the hydrothermal method is suitable for producing nanostructures on large-area patterns. The dandelion nanostructure in this study is a combination of PS nanospheres and ZnO nanorods (Fig. 1(c)). This dandelion structure forms an antireflection layer that enhances light absorption and reduces light reflection in the broadband and omnidirectional spectral range.

Experimental

The multi-layered structure of the proposed CIGS solar cell was fabricated using Mo/CIGS/CdS/i-ZnOAl-doped ZnO (AZO) on a soda-lime glass substrate (Fig. 1(a)). The approximately 1 μm-thick Mo electrode was deposited by a direct current (dc) magnetron sputtering system. The co-evaporation technique was then used to grow a 2 μm-thick CIGS absorber layer. A 50–60 nm-thick CdS buffer layer was then deposited using the chemical bath deposition (CBD) technique. A highly resistive i-ZnO layer between the CdS and ZnO:Al layers was deposited by radio frequency (RF) magnetron sputtering to reduce leakage current. Finally, the 600 nm-thick AZO layer was deposited by RF magnetron sputtering and the top electrode of the Al grid was deposited by thermal evaporation as a transparent conducting oxide.

After the fabrication of the CIGS solar cells, PS nanospheres were patterned on CIGS solar cells (Fig. 1(b)). This study presents an analysis of the optical characteristics of CIGS solar cells with PS nanospheres in a broad spectral range using the rigorous coupled-wave analysis (RCWA) method. The CIGS thin film solar cell structure was simulated by applying the experimental results using 3D simulation (DiffractMod, Rsoft Corp.). Following previous research, physical information regarding the constituent materials, including their refractive indices and extinction coefficients, was used in the numerical modeling of a CIGS solar cell.[24] All simulations were performed under a 1-sun standard air mass 1.5 global (AM1.5G, 100 mW cm^{-2}) light spectrum. Theoretical calculations revealed the optimization of PS nanospheres on the CIGS solar cell. A monolayer of self-assembled PS nanospheres with a plurality of 10 wt% was spun onto the surface, producing a closely packed PS nanospheres monolayer.

A two-step method was used to fabricate ZnO nanorods on the surface of the nanospheres on the CIGS solar cell. This method involves the fabrication of seed layers and growth of nanorods. First, a 100 nm thick AZO layer was deposited by radio frequency (RF) magnetron sputtering to form a seed layer for growing ZnO nanorods. Second, ZnO nanorods were grown by the hydrothermal method. The aqueous solution was prepared by mixing the same concentration of 0.03 M zinc nitrate hexahydrate ($Zn(NO_3)_2 \cdot 6H_2O$, Aldrich) and hexamethylenetetramine ($C_6H_{12}N_4$, HMT, Aldrich) for growing ZnO nanorods. In the hydrothermal method, the chemical reactions related to the fabrication of the ZnO nanorods are as follows:

$$C_6H_{12}N_4 + 6H_2O \rightarrow 6HCHO + 4NH_3 \quad (1)$$

$$NH_3 + H_2O \rightarrow NH_4^+ + OH^- \quad (2)$$

$$Zn^{2+} + 2OH^- \rightarrow Zn(OH)_2 \quad (3)$$

$$Zn(OH)_2 \rightarrow (\text{heat}) \rightarrow ZnO + H_2O \quad (4)$$

After the two aqueous solutions were mixed, solar cells were immersed into the solution at 90 °C for 5 h. Finally, deionized water was used to clean the cell, which was heated at 60 °C in air for 1 h to complete the process of growing the ZnO nanorods.

The morphologies of the fabricated ZnO nanostructures on cells were observed using a field emission scanning electron microscope (FESEM, Hitachi S-4700I). To characterize the performance of the AR coating on the CIGS solar cell, the reflection spectra and angle-dependent reflectance of the samples were measured using a UV-vis-NIR spectrophotometer at wavelengths ranging from 400 to 1000 nm and incident angle from −60 to 60°. The performance of CIGS solar cells was characterized under simulated AM1.5G illumination with a power of 1000 W m^{-2}. The external quantum efficiency (EQE) results were acquired from a system using a 300 W xenon lamp (Newport 66984) light source and a monochromator (Newprot 74112). The beam spot size at the sample measured was approximately 1 mm × 3 mm. The temperature was controlled at 25 ± 1 °C during the measurements.

Results and discussion

The results of the numerical modeling using the RCWA method were used to optimize the PS nanosphere dimensions and obtain a better antireflection effect for a high efficiency CIGS solar cell (Fig. 2). This simulation evaluates the optical performance of periodic structures. The simulated unit cell consists of a hexagonal array, and the simulated structural parameters

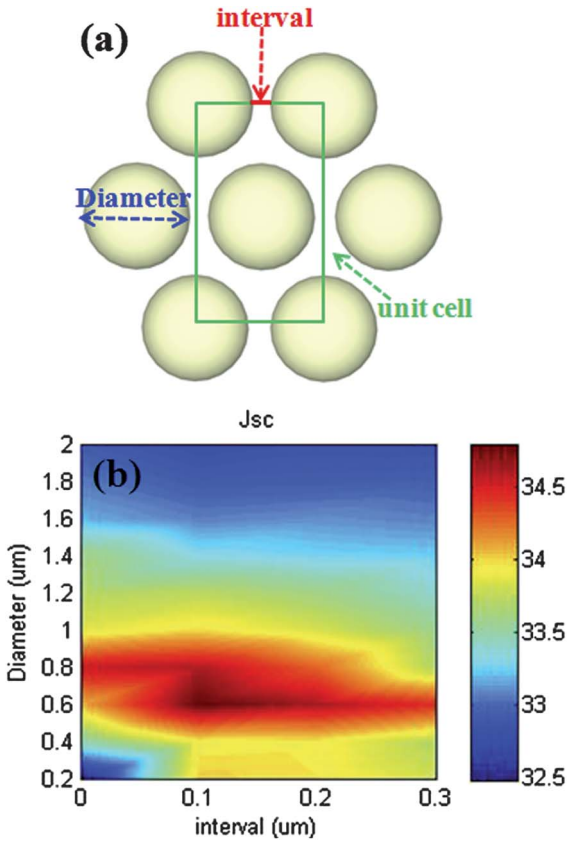

Fig. 2 (a) Top view of one unit cell in a periodic structure. (b) The calculated short-circuit current density J_{sc} (mA cm^{-2}) as a function of the diameter and interval.

include the interval and diameter of the spheres (Fig. 2(a)). Fig. 2(b) shows the short-circuit current density (J_{sc}) of the CIGS solar cells with various distributions and dimensions of PS nanospheres. The surface reflectance was calculated as a function of the nanosphere diameter varying between 200 nm and 2000 nm, and the interval between the nanospheres ranged from 0 nm to 300 nm. Assuming the absorption of photons can be transferred to be electrons completely, the resulting of J_{sc} was calculated using the following equation:

$$J_{sc} = \frac{e}{hc} \int_{400nm}^{1000nm} \lambda[1 - R(\lambda)] I_{AM1.5G}\, d\lambda \quad (5)$$

where e is the electron charge, h is the Planck constant, λ is the wavelength, $R(\lambda)$ denotes the calculated reflectivity for wavelengths between 400 and 1000 nm, and $I_{AM1.5G}$ is the intensity of the AM1.5 G solar spectrum. This simulation also considers multiple reflection and interference. This simulation revealed the optimized J_{sc} for PS nanospheres with a 600 nm diameter and an interval of 100 nm between the nanospheres. Moreover, it is noteworthy that J_{sc} of the CIGS solar cells with the PS nanosphere of 600 nm diameter is higher in the range of 200 to 2000 nm diameter in spite of interval variation. For the extra scattering of the nanospheres to increase the light path length, it is necessary to modulate the period of nearly close-packed 600 nm PS nanospheres to spin onto the surface using the self-assembled method.

Fig. 3 shows the surface morphology of a CIGS solar cell with PS nanospheres and dandelion structures. Monolayers of 600 nm diameter nanospheres were formed by drying the suspension, and Fig. 3(a) shows the layout of PS nanospheres with a closely packed hexagonal pattern. After fabrication of 100 nm thick seed layers on the PS nanospheres, ZnO nanorods were grown on the PS nanospheres (Fig. 3(b)). Fig. 3(b) further shows that when the nanorods were grown on the nanospheres using the hydrothermal method, the PS nanospheres could be protected from collapsing by inserting an AZO seed layer. The ZnO nanorods had diameters of approximately 50 nm and lengths ranging from 600 nm to 800 nm (Fig. 3(c)). Because the seed layer was attached directly to the surface of nanospheres, the ZnO formed omnidirectional nanorods on the nanospheres. The cross-sectional SEM image of the CIGS solar cell in Fig. 3(d) suggests that diameters of 600 nm holes were produced by PS nanospheres collapsing.

To determine the AR performance of the nanospheres and dandelion structures in the 400–1000 nm range, the reflectance spectrum was measured for normal light incidence with a standard UV-vis spectrometer and an integrating sphere (Fig. 4(a)). These results suggest that the PS nanosphere pattern on the CIGS solar cell surface caused the principle reflectance decrease. Specifically, the wavelength of 600–760 nm is obvious. These results suggest that the periodic PS nanospheres can achieve great light harvesting by increasing the path length, and can create efficient light scattering into the CIGS solar cell. After growing the dandelion structures on the PS nanospheres, the amplitude of the interference fringe in the visible range (400 to 800 nm) faded. Besides, effective decrease in reflectance characteristic was observed. This is primarily because the structural profile of ZnO nanorods has a gradient refractive index profile, which acts as a porous layer and buffers the index discontinuity between the air and the cell, reducing the Fresnel reflection.

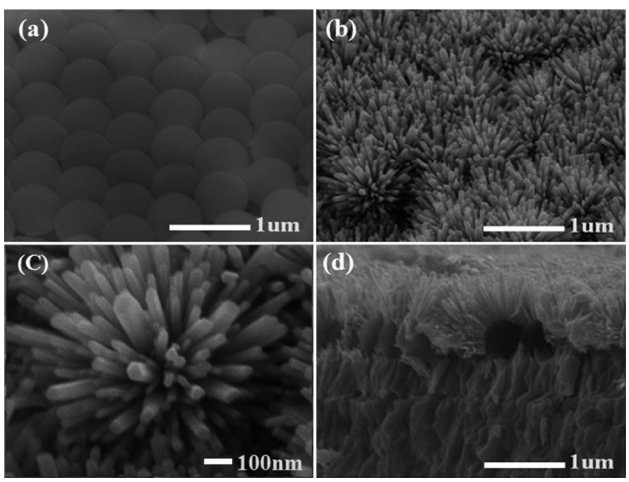

Fig. 3 SEM images of the nanostructures pattern on flat CIGS solar cells: (a) with PS nanospheres, (b and c) with low and high magnification views of ZnO dandelion structures, and (d) cross-sectional SEM image of the CIGS solar cell with ZnO dandelions.

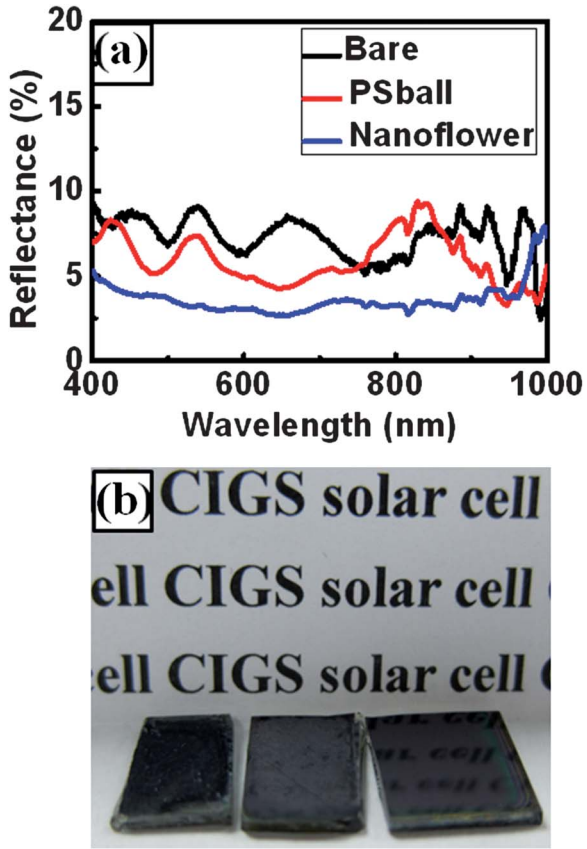

Fig. 4 (a) Reflectance measurements of PS nanospheres and dandelion patterns on CIGS solar cells compared with bare ones. (b) Images of (left) the CIGS solar cell with ZnO dandelion arrays (median) with PS nanospheres and (right) the bare CIGS solar cell.

Additionally, previous theoretical papers have consistently adopted the effective medium theory (EMT) to describe the optical properties of sub-wavelength structures.[25] These studies simulate sub-wavelength structures as effective multi-layered stacks, in which the refractive index gradually decreases from the device surface to the air. Therefore, this study adopts the EMT to explain how the ZnO nanorods efficiently suppressed Fresnel reflection. The effective refractive index (n_{eff}) of the ZnO nanorods can be obtained using the following weighting formula:

$$n_{\text{eff}} = \left[{n_{\text{ZnO}}}^2 \times f + {n_{\text{air}}}^2(1-f)\right]^{\frac{1}{2}} \quad (6)$$

where f is the filling factor of the ZnO nanorods, and n_{ZnO} and n_{air} are refractive indices of ZnO and air, respectively. In these calculations, the refractive index of ZnO is approximately 2.1, and the filling factor of the ZnO nanorods was estimated by the SEM images. For the unit dandelion structures, the filling factors of the top and bottom of ZnO nanorod structures were 0.39 and 1, and the n_{eff} values were calculated as 1.52 and 2.1, respectively. Because of the length variation of the ZnO nanorods (Fig. 3(c)), the nanorod filling factor varies with the depth. Therefore, cells with a dandelion structure have the lowest reflection because the nanorods leading to the effective refractive index profile grade more continuously in the air to the surface of cell. Consequently, this study proposes that the dandelion structure is suitable for AR coating of CIGS solar cells.

Fig. 4(b) shows images of a bare CIGS solar cell, a CIGS solar cell with PS nanospheres, and one with a dandelion structure. The reflection of the words printed on the paper imaged on the cells was used to investigate the reflection characteristics of the AR-coated cells. The patterned PS nanospheres degraded the brightness of the reflection characteristics compared to the bare cell, whereas the colors of the cells with dandelion structures were much blacker than those with the PS nanospheres. These results are in agreement with the reflectance shown in Fig. 4(a).

Because of the sun movement, an anti-reflection coating should reduce reflection and increase the transmission into the absorption layer omnidirectionally. To further understand the omnidirectional AR characteristics, this study measures the angle-dependent reflection of the CIGS solar cells. Fig. 5(a–c) show the measured angle-dependent reflectance of CIGS solar cells with flat (bare cell), nanosphere, and dandelion structures, respectively. Angle-dependent mappings of the CIGS solar cells were performed at incident angles ranging from −60° to 60°. The reflectance spectra were measured at wavelengths from 400 to 1000 nm. The reflectance values are represented by the color bars, where red and blue colors represent low to high reflectance. Fig. 5(a) shows that the reflection of a bare CIGS solar cell has the amplitude of the interference fringe in the visible range, and the bare cell exhibits higher reflection at 55–60°. The reflection decreased when PS nanospheres were patterned on the CIGS solar cell surface at the normal incidence, but the reflection at wavelengths between 400 and 650 nm and the incidence angles of 55–60° became higher. However, the reflection decreased omnidirectionally when the ZnO nanorods were grown on the PS nanospheres. This is because different reflectance behaviors are attributable to the gradual refractive index from the cell surface to the air. Consequently, in the angle-dependent mappings, the CIGS solar cell with the dandelions structures shows the lowest reflectance. This cell not only successfully reduces the broadband reflectivity at the normal incidence, but also reduces reflectance for incident angles between −60° and 60°.

To investigate the effect of solar power harvest for an entire day, the solar-spectrum (AM1.5G) weighted reflectance (SWR) was estimated by the reflectance spectra and the solar spectral photon flux integrated over a wavelength range of 400–1000 nm. This study defines the SWR to express the antireflective power of the structures as the following:

$$\text{SWR} = \frac{\int_{400\text{nm}}^{1000\text{nm}} R(\lambda) I_{\text{AM1.5G}}(\lambda)\,\text{d}\lambda}{\int_{400\text{nm}}^{1000\text{nm}} I_{\text{AM1.5G}}(\lambda)\,\text{d}\lambda} \quad (7)$$

where $R(\lambda)$ is the measured reflectivity and $I_{\text{AM1.5G}}$ is the photon flux density of the AM1.5G solar spectrum. The weighted reflectance of the bare CIGS cell was approximately 7.64%, whereas the weighted reflectance of the CIGS cell with a PS nanospheres pattern on the surface decreased to 5.97%. Finally,

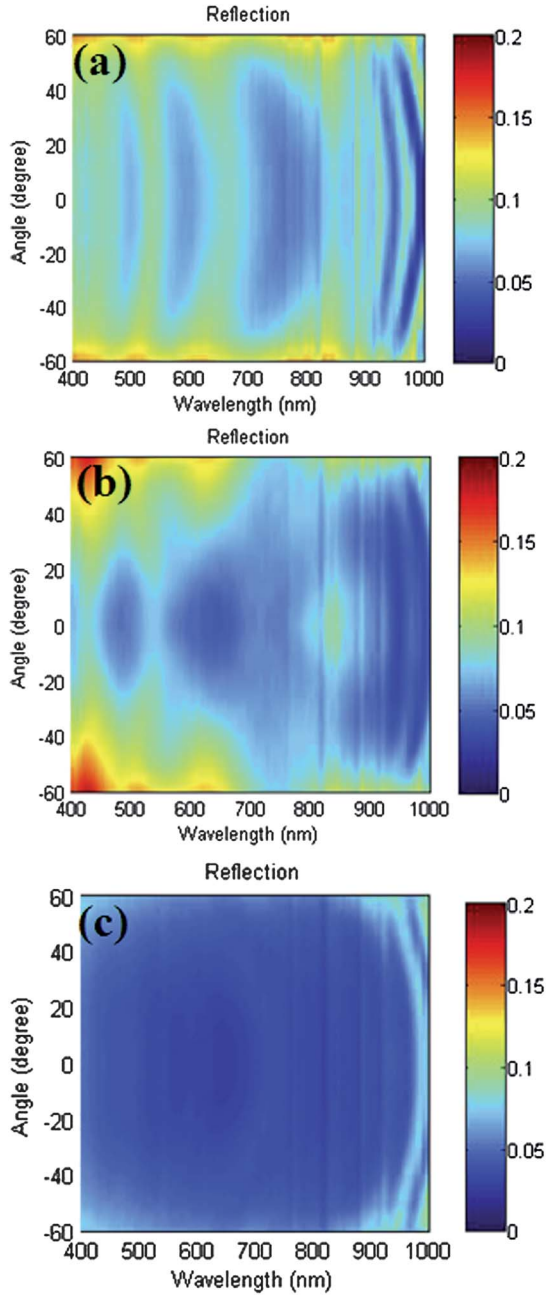

Fig. 5 The measured angular reflectance spectra for solar cells with (a) bare, (b) PS nanospheres, and (c) dandelions.

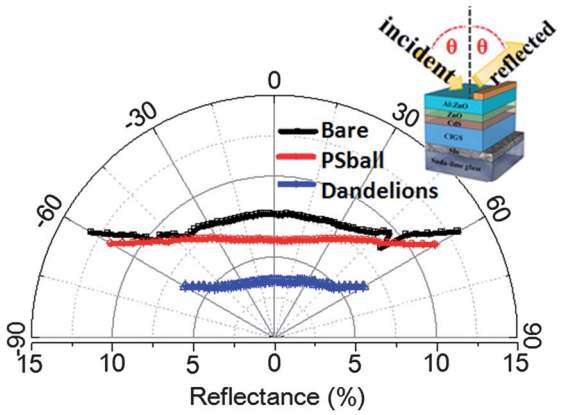

Fig. 6 The weighted reflectance of all cells.

the weighted reflectance decreased to 3.64% when the dandelion structures were grown on the surface of the PS nanospheres. Fig. 6 shows the weighted reflectance of the dandelion cell, exhibiting an excellent decrease at every incident angle compared to the bare cell and nanosphere cell. The weighted reflectance of the dandelion cell is still less than 5% at an incident angle of 45°, and 7% at an incident angle of 60°. Therefore, this study shows that ZnO dandelions are suitable for creating an omnidirectional AR coating for CIGS solar cells. Fig. 7(a) shows the photovoltaic *I–V* characteristics at the normal incident angle. The CIGS solar cell with ZnO dandelion structures was tested under standard test conditions with simulation air mass 1.5 global illumination. This study also compares this cell with a standard one without any AR structures.

The short-circuit density (J_{sc}) of the solar cell with the ZnO dandelion structure increased from 22.7 mA cm^{-2} to 25.26 mA cm^{-2}, differing by an additional 2.56 mA cm^{-2}. The photocurrent enhancement factor ($EF_{J_{sc}}$) was 11.27%, as calculated by

$$EF_{J_{sc}} = \frac{\Delta J_{sc}}{J_{sc}} = \frac{J_{sc}(\text{with ARc}) - J_{sc}(\text{without ARc})}{J_{sc}(\text{without ARc})} \quad (8)$$

The antireflection effect of ZnO dandelions enhanced the power conversion efficiency from 10.35% to 11.14% because of the increase in the short-circuit current. The quantum efficiency (EQE) measurement shown in Fig. 7(b) also supports the enhancement of conversion efficiency created by the ZnO dandelion structure. Compared to the bare cell, the CIGS solar cell with dandelion structures demonstrates an enhanced photoresponse for wavelengths ranging from 410 to 980 nm. This observation confirms that the improvement in J_{sc} of the CIGS solar cell with dandelion structures compared with the bare one is because of the great antireflection property of the dandelion structures. However, the ZnO dandelion structures also exhibit absorption below 410 nm, affecting the EQE slightly. The fill factor also decreases slightly, suggesting that ZnO dandelion structures grown on the surface of the device do not affect residual series resistance and the conductance of electrons in the emitter layer. The angle-dependent conversion characteristic is further investigated by a homemade rotatable photo *I–V* measurement. Fig. 7(c) shows the angular short-circuit current density and corresponding $EF_{J_{sc}}$ for the cells with and without dandelion structures. As Fig. 7(c) shows, the incident angles are between −60° and 60°. When the cells are measured under the normal incident angle, the photocurrent enhancement factor of dandelion structure cells is 11.27%. However, as the light incident angle increased to 60° (or −60°), the $EF_{J_{sc}}$ increased to 31.87%. This result implies that $EF_{J_{sc}}$ improves as the light incident angle increases. Therefore, the superior antireflection capability over a wide range of incident angles can further improve the solar energy conversion efficiency for the entire day, and integrating the 1D ZnO nanorods

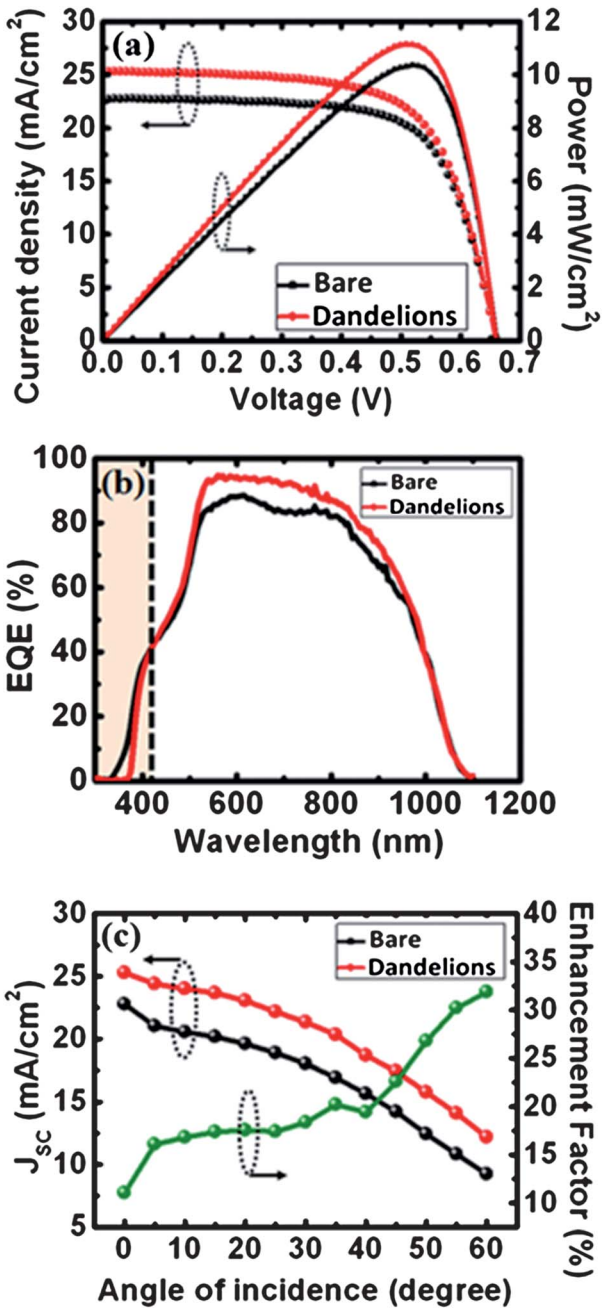

Fig. 7 (a) The current density–voltage curves and (b) the external quantum efficiencies of the solar cell with dandelion structures and the bare cell. (c) The angular photocurrent characterization of the solar cell with dandelion structures and the bare cell. The green curve shows the corresponding enhancement factor at different incident angles.

with the PS nanospheres has the potential to provide enhanced broadband and omni-directional antireflective properties.

Conclusions

In summary, a CIGS solar cell with a dandelion structure was fabricated and characterized in detail. The weighted reflectance of the CIGS solar cell with ZnO dandelion arrays decreased significantly to 3.64%, as calculated over a wavelength range of 400–1000 nm. Therefore, the photocurrent density increases from 22.7 mA cm^{-2} to 25.26 mA cm^{-2}, differed by an additional 2.56 mA cm^{-2}. The power conversion efficiency increased from 10.35% to 11.14%. For the omnidirectional AR characteristics, the weighted reflectance of the cell with a dandelion structure was still less than 5% at an incident angle of 45°, and 7% at an incident angle of 60°. The angular *I–V* characterization confirms an enhanced photocurrent conversion for an incident angle up to 60°. Additionally, as the light incident angle increased to 60°, the $EF_{J_{sc}}$ increased to 31.87%. Because of the cost-efficient and low-temperature fabrication process, and superior AR properties across a broad spectral range and angles of incidence, this study proposes that dandelion arrays can form a suitable AR layer for electro-optical devices.

Acknowledgements

This work was also supported by the Green Technology Research Center of Chang Gung University and the National Science Council (NSC) of Taiwan under contract no. NSC101-2112-M-182-003-MY3 and NSC101-3113-E-182-001-CC2.

Notes and references

1 K. M. Yeung, W. C. Luk, K. C. Tam, C. Y. Kwong, M. A. Tsai, H. C. Kuo, A. M. C. Ng and A. B. Djurisic, *Sol. Energy Mater. Sol. Cells*, 2011, **95**, 699–703.
2 A. Chirilă, S. Buecheler, F. Pianezzi, P. Bloesch, C. Gretener, A. R. Uhl, C. Fella, L. Kranz, J. Perrenoud, S. Seyrling, R. Verma, S. Nishiwaki, Y. E. Romanyuk, G. Bilger and A. N. Tiwari, *Nat. Mater.*, 2011, **10**, 1–5.
3 L. Zhang, Q. He, W. L. Jiang, F. F. Liu, C. J. Li and Y. Sun, *Sol. Energy Mater. Sol. Cells*, 2009, **93**, 114–118.
4 EMPA, *A new world record for solar cell efficiency*, http://www.empa.ch/plugin/template/empa/3/131438/—/l=2, 2013.
5 B. S. Richards, *Prog. Photovolt: Res. Appl.*, 2004, **12**, 253–281.
6 V. M. Aroutiounian, K. Martirosyan and P. Soukiassian, *J. Phys. D: Appl. Phys.*, 2006, **39**, 1623–1625.
7 P. Lalanne and G. M. Morris, *Proc. SPIE*, 1996, **2776**, 300.
8 S. H. Baek, S. B. Kim, J. K. Shin and J. H. Kim, *Sol. Energy Mater. Sol. Cells*, 2012, **96**, 251–256.
9 C. H. Sun, P. Jiang and B. Jiang, *Appl. Phys. Lett.*, 2008, **92**, 061112.
10 P. C. Tseng, P. C. Yu, H. C. Chen, Y. L. Tsai, H. W. Han, M. A. Tsai, C. H. Chang and H. C. Kuo, *Sol. Energy Mater. Sol. Cells*, 2011, **95**, 2610–2615.
11 M. A. Tsai, H. W. Han, Y. L. Tsai, P. C. Tseng, P. Yu, H. C. Kuo, C. H. Shen, J. M. Shieh and S. H. Lin, *Opt. Express*, 2011, **19**, A757–A762.
12 O. Gunawan, K. Wang, B. Fallahazad, Y. Zhang, E. Tutuc and S. Guha, *Prog. Photovolt: Res. Appl.*, 2011, **19**, 307–312.
13 H. Ng, J. Han, T. Yamada, P. Nguyen, Y. Chen and M. Meyyappan, *Nano Lett.*, 2004, 1247–1252.
14 M. Huang, C. Yang, Y. Chiou and R. Lee, *Sol. Energy Mater. Sol. Cells*, 2008, **92**, 1352–1357.
15 B. Fuhrmann, H. S. Leipner, H. Höche, L. Schubert, P. Werner and U. Gösele, *Nano Lett.*, 2005, **5**, 2524–2527.

16 M. C. Putnam, S. W. Boettcher, M. D. Kelzenberg, D. B. Turner-Evans, J. M. Spurgeon, E. L. Warren, R. M. Briggs, N. S. Lewis and H. A. Atwater, *Energy Environ. Sci.*, 2010, **8**, 1037–1041.
17 L. Tsakalakos, J. Balch, J. Fronheiser, B. A. Korevaar, O. Sulima and J. Rand, *Appl. Phys. Lett.*, 2007, **91**, 233117.
18 M. K. Kim, D. K. Yi and U. Paik, *Langmuir*, 2010, **26**, 7552–7554.
19 Y. H. Zheng, L. R. Zheng, Y. Y. Zhan, X. Y. Lin, Q. Zheng and K. M. Wei, *Inorg. Chem.*, 2007, **46**, 6980–6986.
20 M. Y. Hsieh, S. Y. Kuo, H. V. Han, J. F. Yang, Y. K. Liao, F. I. Lai and H. C. Kuo, *Nanoscale*, 2013, DOI: 10.1039/C3NR34079A.
21 M. S. Samuel, J. Koshy, A. Chandran and K. C. George, *Curr. Appl. Phys.*, 2011, **11**, 1094–1099.
22 J. X. Wang, C. M. L. Wu, W. S. Cheung, L. B. Luo, Z. B. He, G. D. Yuan, W. J. Zhang, C. S. Lee and S. T. Lee, *J. Phys. Chem. C*, 2010, **114**, 13157–13161.
23 H. C. Chen, C. C. Lin, H. W. Wang, M. A. Tsai, P. C. Tseng, Y. L. Tsai, H. W. Han, Z. Y. Li and Y. A. Chang, *IEEE Photonics Technol. Lett.*, 2011, **23**(11), 691–693.
24 S. Y. Kuo, M. Y. Hsieh, F.-I. Lai, Y. K. Liao, M. H. Kao and H. C. Kuo, *Jpn. J. Appl. Phys.*, 2012, **51**, 10NC14.
25 J. Zhong, H. Chen, G. Saraf, Y. Lu, C. K. Choi, J. J. Song, D. M. Mackie and H. Shen, *Appl. Phys. Lett.*, 2009, **07**, 203515.

